Nanoscale Advances

ROYAL SOCIETY OF CHEMISTRY

PAPER

View Article Online
View Journal | View Issue

Cite this: *Nanoscale Adv.*, 2021, **3**, 1096

Molecular engineering for high-performance fullerene broadband photodetectors†

Mingming Su, Yajing Hu, Ao Yu, Zhiyao Peng, Wangtao Long, Shixin Gao, Ping Peng,* Bin Su and Fang-Fang Li *

Broadband photodetectors fabricated with organic molecules have the advantages of low cost, high flexibility, easy processing and low-temperature requirement. Fullerene molecules, due to their electron accepting and photoinduced electron transfer properties, are potential materials for photodetectors. However, fullerene has a narrow light absorption spectrum range, and realization of large-area fullerene-based broadband photodetectors remains a challenge. Herein, we broaden the absorption wavelength range of fullerene through molecular engineering, *i.e.* adding a donor molecule, nickel tetraphenylporphyrin (NiTPP) with strong visible light absorption capacity, onto the fullerene cage to form a donor–acceptor dyad (NiTPP-C_{60}). Moreover, large-area nickel porphyrin–fullerene (NiTPP-C_{60}) single-crystal arrays were prepared by applying a liquid-bridge induced assembly method. Combining the excellent visible light absorption properties of porphyrin and the good electron transport characteristic of fullerene, photodetectors fabricated with NiTPP-C_{60} single-crystal arrays show a fast photoelectric response with τ_{on} < 0.09 s at 350 nm, τ_{on} < 0.10 s at 425 nm and τ_{on} < 0.08 s at 530 nm, and the highest responsivity of 11.9 A W^{-1} at 425 nm. This study provides a new strategy toward the fabrication of high-performance fullerene broadband photodetectors and presents a versatile method for the design of large-area well-aligned organic single-crystal arrays for practical electronic applications.

Received 24th November 2020
Accepted 30th December 2020

DOI: 10.1039/d0na00981d

rsc.li/nanoscale-advances

1. Introduction

Photodetectors are devices that convert light signals into electrical signals, which have broad applications in optical interconnection techniques, light-wave communications, circuits, and high-resolution imaging.[1–5] According to the working wavelength range, photodetectors are generally classified into narrowband photodetectors and broadband photodetectors. Narrowband photodetectors can accurately detect a specific light through material selection and optical path design. Broadband photodetectors have a wide detection range, and a single device can achieve multi-spectral detection functions. With the increasing application requirements, photodetectors that can only detect a single wavelength no longer satisfied the criteria for multiple detections. Although assembling multiple sets of narrowband detection systems could be applicable, it is costly due to the device packaging and chip integration. Therefore, researchers have paid attention to broadband photodetectors to control the integration cost and simplify the assembly process, and applied them in digital photography, optical sensing, and night vision applications.[6–13]

Traditional broadband photodetectors are prepared from inorganic semiconductor materials (such as Si, MoS_2 and InGaAs), whereas, the materials are expensive and the manufacturing process is complicated.[14,15] Compared to inorganic semiconductors, organic small-molecule semiconductors have attracted considerable attention in optical detection applications, because of their cost-effectiveness, flexibility, amenability to roll-to-roll large area producing, compatibility with plastic substrates, tunable molecular structures, and broader light range response.[13,16–20]

Fullerene (C_{60}), as an electron acceptor with fast photoinduced charge transfer properties, is a promising candidate for organic photodetectors. For example, C_{60} single-crystal arrays and microribbons have been prepared through solvent-assisted methods and exhibited an excellent photoresponse and high photoresponsivity.[21,22] However, the weak visible light absorption and high electronic transition energy levels (HOMO → LUMO) of C_{60} limit its application in broadband photodetectors. To realize a fullerene broadband photodetector, a material with strong absorption in the visible light region was selected to form a heterojunction with fullerene, thereby broadening the absorption spectrum of the device.[23–26] For example, Peng and co-workers successfully achieved an excellent broadband optical response from the ultraviolet to the near-infrared region by constructing a fullerene (C_{60})/AlClPc planar heterojunction structure.[23] It showed a high responsivity of 94.4 A W^{-1}, and

State Key Laboratory of Materials Processing and Die & Mould Technology, School of Materials Science and Engineering, Huazhong University of Science and Technology, Wuhan 430074, China. E-mail: ppeng@hust.edu.cn; ffli@hust.edu.cn

† Electronic supplementary information (ESI) available. See DOI: 10.1039/d0na00981d

a detectivity of ~1.5×10^{13} Jones. Gong *et al.* prepared a bulk heterojunction structure based on a donor–acceptor (D–A) conjugated polymer PBBTPD and tri-$PC_{61}BM$, which achieved light detection in the wavelength range from 350 nm to 2500 nm, and showed a responsivity of 5×10^{-2} mA W^{-1} at 800 nm and detectivity higher than 10^{11} Jones.[27] Lu *et al.* fabricated a planar heterojunction of CuPc/C_{60}, which exhibited a responsivity of 0.094 A W^{-1}.[25] However, the contact area between the donor and acceptor in a planar heterojunction structure is small, which greatly limits the photoelectric conversion efficiency of the device. For bulk heterojunction structures, the transportation of charge carriers to the electrode is sensitive to the morphology and particle size of the material.[28] A large particle size will result in a small contact interface area of the donor and acceptor and low efficiency of exciton dissociation, while, if the particle size is too small, the numbers of particles will increase and the transportation of carriers will be restricted.

Thus, we propose to connect an electron donor unit possessing strong absorption in the visible light region to fullerenes to form a single-molecule D–A intramolecular heterojunction. In this way, the excitons generated by light absorption are dissociated inside the molecules, and the generated carriers are also transported within the molecules, which fundamentally avoid the influence of phase separation between the donor and acceptor on the dissociation of excitons.[29–35] Porphyrin molecules are macrocyclic conjugated electron-rich compounds that can act as electron donors and exhibit strong absorption in the visible light region.[36,37] By contrast, fullerenes are electron-deficient molecules that can act as electron acceptors[38] and show strong absorption in the UV region. Modification of a fullerene cage with a porphyrin structure through covalent bonds to form a D–A dyad molecule could realize broad spectral absorption. Moreover, fullerene–porphyrin dyads were found to exhibit photoinduced electron transfer properties,[39–42] making them promising candidates for broadband photodetectors.

The photoelectric performance of fullerenes depends heavily on their morphology and crystallinity. Highly ordered crystalline fullerene micro/nano-structures can dramatically enhance the photoresponse performance. One-dimensional (1D) crystalline fullerene structures are of particular interest for optoelectronic devices due to the presence of effective channels for charge transportation, enabling a superior optical and electrical response.[43,44] However, the preparation of large-area and highly ordered fullerene micro/nanostructure arrays is challenging and has rarely been reported. One-dimensional fullerene structures obtained from the solution process are generally discontinuous C_{60} crystals or oriented in one direction at a random position,[44–46] which is unfavorable for the fabrication of large-scale integrated devices and impedes their practical applications. Thus, the synthesis of large-area and long-distance ordered fullerene-porphyrin dyad single crystalline arrays is desirable for high-performance broadband photodetectors.

In this work, a fullerene–nickel tetraphenylporphyrin dyad (NiTPP-C_{60}) was synthesized and assembled to a large-area single-crystal microwire array by the "liquid bridge induced assembly" (LBIA) method.[47–49] For comparison, crystalline microwire arrays of C_{60} and NiTTP with different concentrations were prepared as well. The average width of the microwires increases with fullerene concentrations. Attributed to the complementary spectra of C_{60} and NiTPP in the UV-Vis region, the devices fabricated with NiTPP-C_{60} microwire arrays as a light-absorbing layer show an excellent broad-spectral response. The performances of the NiTPP-C_{60} photodetector are superior to those of C_{60} and NiTPP detectors. The strategy presented here provides a clue for future design and synthesis of functional fullerenes and their large-scale 1D crystal arrays for broadband photodetectors with a spectral response from the ultraviolet to the visible region and even to the near-infrared region.

2. Results and discussion

The fullerene–porphyrin dyad (NiTPP-C_{60}) was synthesized according to a previous report.[50] UV-vis-NIR spectroscopy is one of the most convenient techniques to study the optical absorption characteristics of materials. Fig. 1 shows the UV-visible absorption spectra of C_{60}, NiTPP, and NiTPP-C_{60} in dichlorobenzene (*o*-DCB). C_{60} exhibits a strong absorption in the ultraviolet region at 336 nm and a weak absorption in the visible region at 404 nm. For NiTPP, a strong absorption peak appears at about 418 nm, which is the Soret absorption band generated by the electron transition of the porphyrin molecule $a_{1\mu}(\pi)$–$e_g(\pi^*)$. Another absorption peak around 530 nm is a Q-band absorption peak generated by an electron transition between the porphyrin molecules $a_{2\mu}(\pi)$–$e_g(\pi^*)$. The absorption spectrum of NiTPP-C_{60} can be seen as a combination of the absorption spectrum of C_{60} and NiTPP. NiTPP-C_{60} exhibits absorptions in the range of 300 to 600 nm, indicating its potential application for broadband photodetectors.

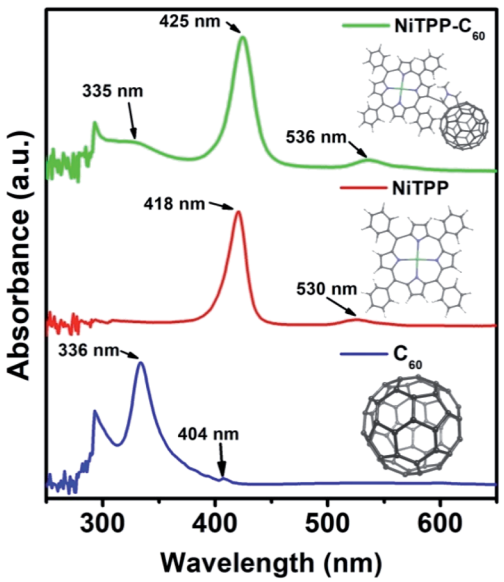

Fig. 1 UV-vis absorption of C_{60}, NiTPP, and NiTPP-C_{60} in *o*-DCB.

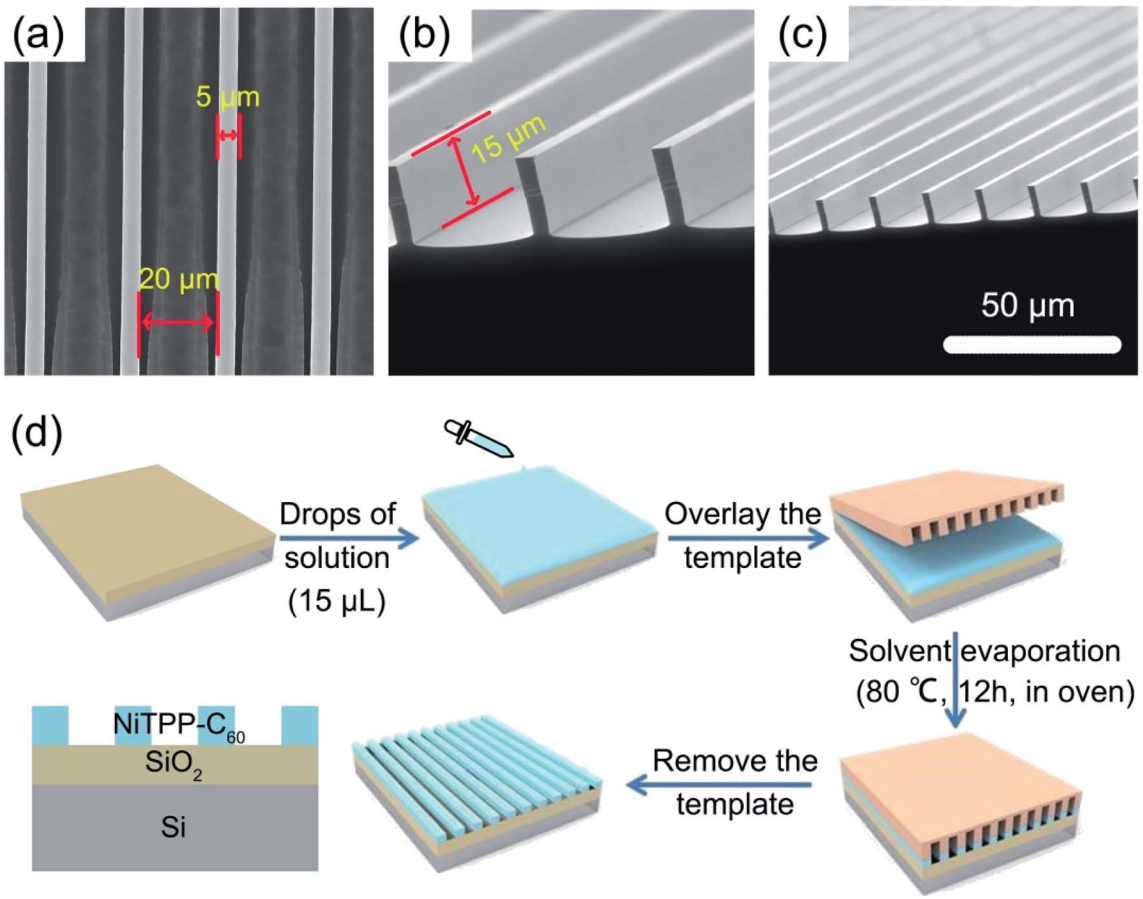

Fig. 2 (a–c) SEM images of an asymmetric infiltrating template. (d) Assembly process of one-dimensional microwire arrays of NiTPP-C_{60}.

To obtain a large-scale photodetector device, a liquid-bridge induced assembly method was applied.[51–53] A designed micropillar template (Fig. 2a–c) was used to prepare large-area microwire arrays. The width and height of the microcolumns are 5 μm and 15 μm, respectively, and the spacing between two adjacent microcolumns is 20 μm. Notably, the sidewall of the microcolumn template is modified with heptafluorododecyltrimethoxysilane (FAS) molecules to make its wettability different from the top, which is a key to microwire crystallization. *o*-Dichlorobenzene (*o*-DCB) was chosen as the solvent to dissolve NiTPP-C_{60} for the subsequent crystallization due to its high solubility for fullerene derivatives and slow evaporation rate. Fig. 2d displays the self-assembly process of the microwire arrays. 15 μl of the NiTPP-C_{60} solution with respective concentrations of 0.5, 1, and 2 mg ml^{-1} was carefully dropped onto the substrate, followed by gentle covering with a template. The assembled device was then put in an oven for evaporation (80 °C). Single-crystal microwire arrays were successfully crystallized after 12 h. During the preparation process, the fullerene solution is confined in the gaps of the microcolumns, and the top of the lyophilic microcolumn is to adjust the position and size of the microwires, which allow fabrication of large-scale, high-crystallinity and highly ordered microwires.[52]

The optical and scanning electron micrographs of the assembled structures of NiTPP-C_{60} display a large-area and orderly arranged microwire array (Fig. 3a–f and S1 in the ESI†). The size of the microwires is uniform and no apparent defects or ruptures are present in SEM and optical images. NiTPP-C_{60} microwires prepared from 1 mg ml^{-1} solution display smoother surfaces and edges than those from 0.5 mg ml^{-1} and 2 mg ml^{-1} NiTPP-C_{60}, which are critical to achieve fast electron transport within the microwire to promote efficient conversion of an optical signal into an electrical signal, thus achieving high device performances. For comparison, the microwire arrays of C_{60}, and NiTPP at the concentrations of 0.5, 1 and 2 mg ml^{-1} were prepared as well by the same procedures as described for NiTPP-C_{60} (Fig. S2 and S3†). It is found that the microwire arrays prepared from 1 mg ml^{-1} solution exhibit better morphology with fewer defects. Notably, the width of microwires is an important parameter for calculating the responsivity of a photodetector, and thus, we prepared five samples at each concentration and randomly selected ten microwires from each sample to count the width. We found that the microwire width is controlled by fullerene concentrations. As the concentration of NiTPP-C_{60} increases from 0.5 to 2 mg ml^{-1}, the major width distribution increases from 3.15 to 3.5 μm (Fig. S4†). The same tendency was observed for C_{60} and NiTPP microwires (Fig. S5†). The width statistics of C_{60}, NiTPP and NiTPP-C_{60} microwires with different concentrations are listed in Table S1.†

The structure of NiTPP-C_{60} microwires prepared from 1 mg ml^{-1} solution has better morphology and was further

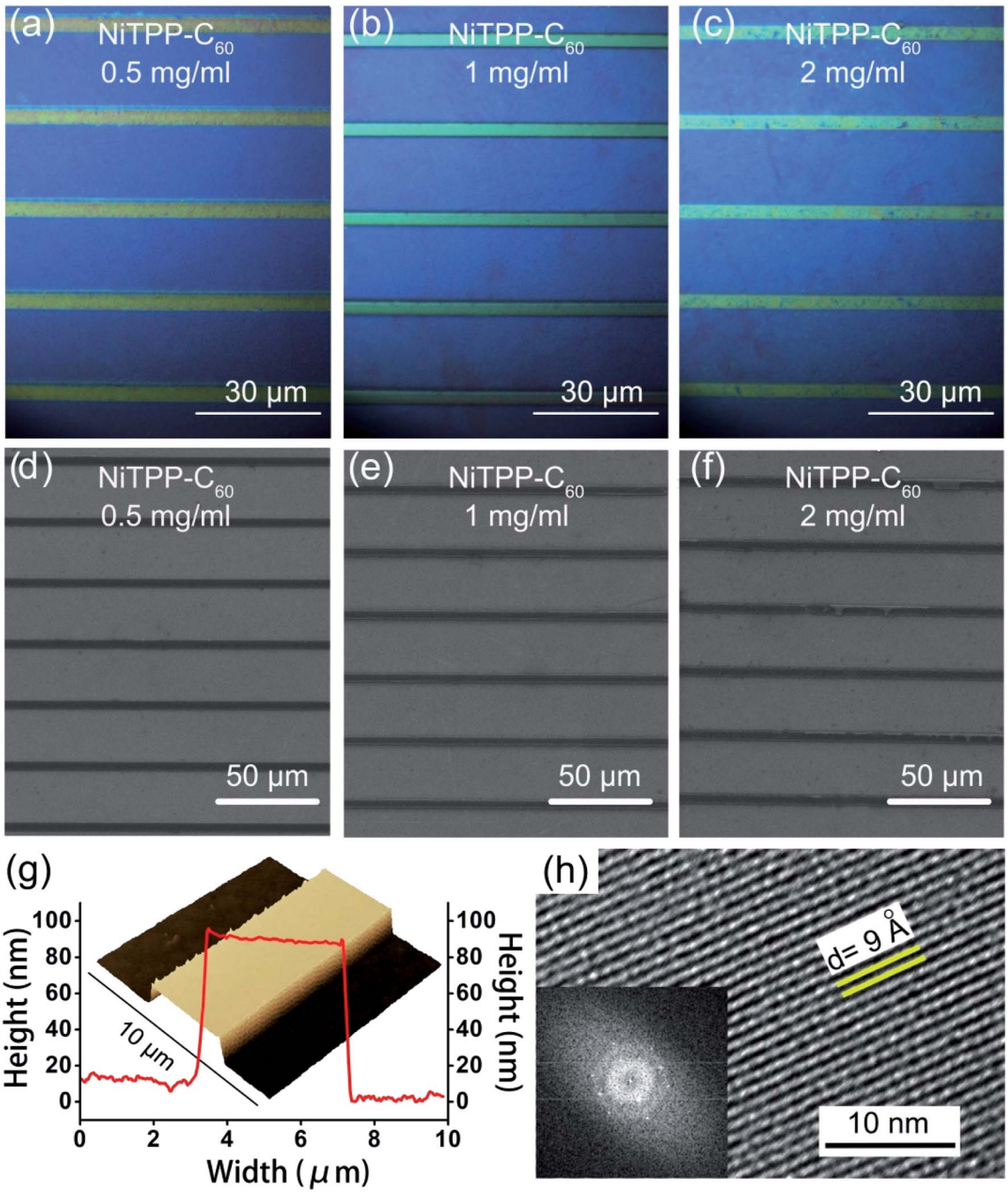

Fig. 3 Optical (a–c) and SEM (d–f) images of NiTPP-C_{60} microwire arrays at concentrations of 0.5 mg ml^{-1}, 1 mg ml^{-1} and 2 mg ml^{-1}, respectively. (g) 3D-AFM and height distribution images of NiTPP-C_{60} microwires at a concentration of 1 mg ml^{-1} (h) HRTEM and corresponding FFT images of NiTPP-C_{60} (1 mg ml^{-1}) microwire.

characterized using a three-dimensional (3D) atomic force microscope (AFM) and HRTEM. As shown in Fig. 3g and S6,† the crystal has a flat, clean, and smooth surface with a uniform thickness of ~90 nm, and the height difference of the microwire in the longitudinal direction is less than 3 nm, which lay the foundation for the high-speed migration of electrons in the microwire.[54] AFM tests on C_{60} and NiTPP microwires prepared from 1 mg ml^{-1} solution were also performed. Both microwires show smooth, flat surfaces and a uniform height of ~90 nm, reflecting the high crystallinity of the microwires (Fig. S7†). The HRTEM image of NiTPP-C_{60} microwires (Fig. 3h) demonstrates the preferred growth orientation of fullerene molecules. It shows clear lattice planes with a measured d value of 9 Å. The fast Fourier transformation (FFT) image (inset image) displays regular single-crystal diffraction spots, implying that the as-formed microwires are highly crystalline.

Photodetection measurements were performed to study the applications of NiTPP-C_{60} microwire arrays in broadband

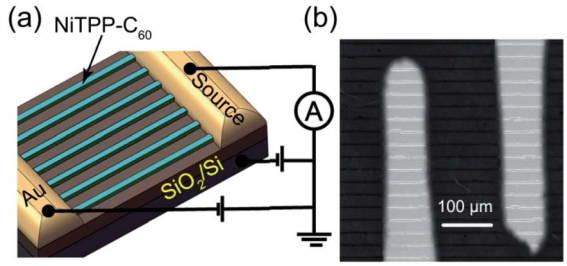

Fig. 4 (a) Schematic diagram of the photodetector device based on microwire arrays grown from 1 mg ml^{-1} NiTPP-C_{60} and (b) SEM images of the corresponding device.

photodetectors. The device structure fabricated with microwire arrays and the corresponding SEM image are shown in Fig. 4. Gold (Au) as an electrode material was deposited on both ends of the microwires by a thermal evaporation method (Fig. 4a). The effective area between two Au electrodes that directly affects the performance of the device can be determined by the width and the valid numbers of microwires. The numbers of effective microwires can be counted through the SEM image in Fig. 4b.

The photocurrent–time (I–T) diagram of the NiTPP-C_{60} microwire device shows long-term stable photoelectric response characteristics under a periodic light stimulation at 350 nm, 425 nm, and 530 nm, respectively (Fig. 5a, c and e). An increase in optical power density can activate more electron–hole pairs in the microwires and lead to a larger photocurrent. The photocurrent under a 425 nm light source (~530 nA) is more significant compared with that under 350 nm (~326 nA) and 530 nm (~150 nA) light sources, which agrees well with the strongest absorption of NiTPP-C_{60} at 425 nm. The fast photoresponse of the detector to the three light sources was

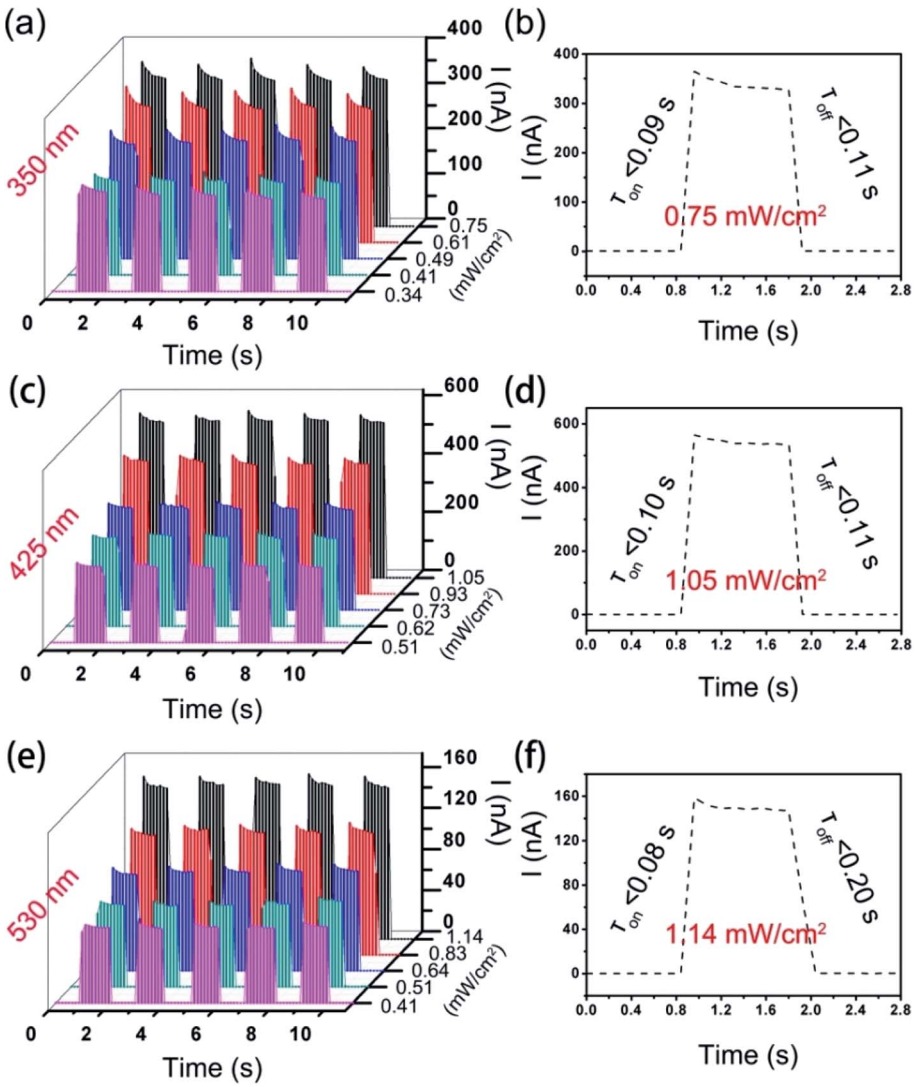

Fig. 5 I–T curves of the NiTPP-C_{60} (1 mg ml^{-1}) microwires measured at room temperature with (a) 350 nm, (c) 425 nm and (e) 530 nm light under different optical power intensities. Single-cycle optical response of the device (b) under 350 nm UV light and 0.75 mW cm^{-2} optical power density, (d) 425 nm light and 1.05 mW cm^{-2} density, (f) 530 nm light and 1.14 mW cm^{-2} density. The effective light-receiving area is 5.84×10^{-5} cm^2 for all photoelectric detection devices, and $V_{GS} = V_{DS} = 10$ V.

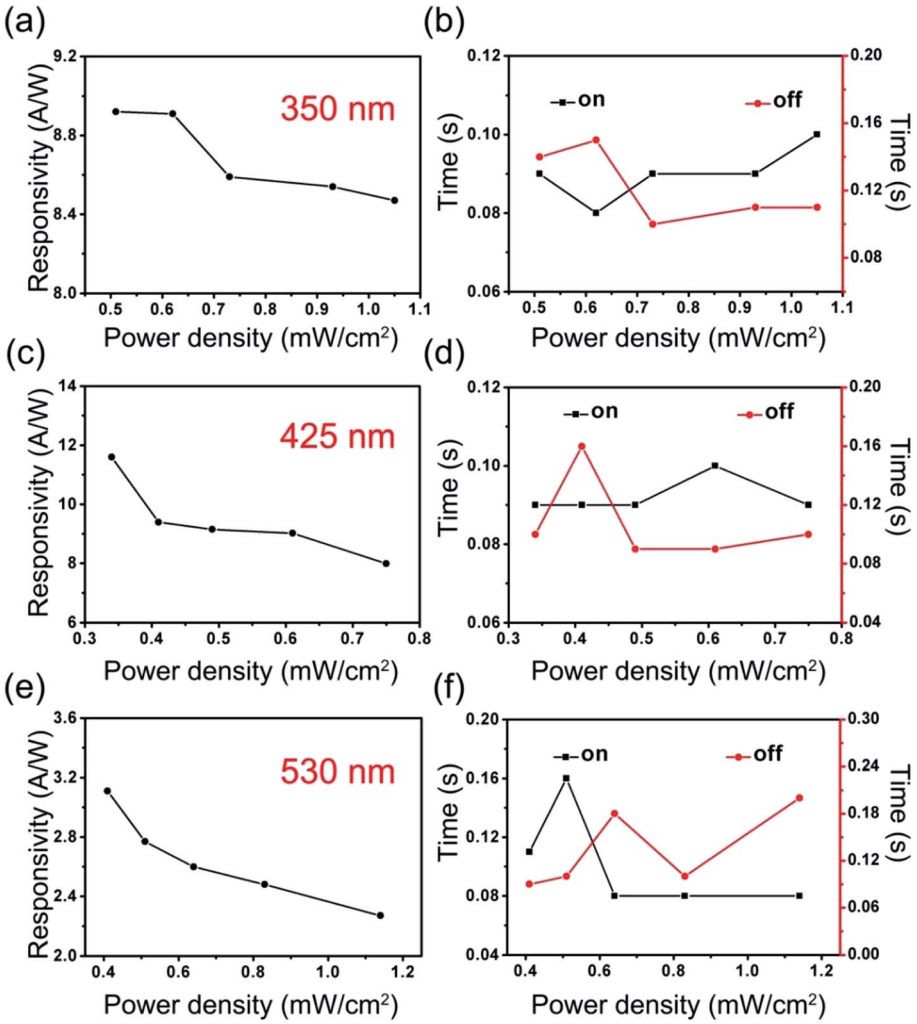

Fig. 6 Responsivity of NiTPP-C_{60} (1 mg ml^{-1}) microwires (a) at 350 nm, (c) 425 nm and (e) 530 nm under different optical power densities. Rise and decay time of NiTPP-C_{60} (1 mg ml^{-1}) microwires (b) at 350 nm, (d) at 425 nm and (f) at 530 nm light under different optical power densities.

demonstrated in the single-cycle *I–T* curves and the response time is 0.08–0.1 s (Fig. 5b: 350 nm, 0.75 mW cm^{-2}; Fig. 5d: 425 nm, 1.05 mW cm^{-2}; Fig. 5f: 530 nm, 1.14 mW cm^{-2}). The photocurrent–voltage (*I–V*) curves of the devices measured in the dark and under irradiation with three wavelength light sources display a linear relationship between the current and voltage (Fig. S8†), indicating that the microwire arrays are in ohmic contact with the gold electrodes, which is favorable for current input and output.

Correspondingly, the photoelectric detection performances of C_{60} and NiTPP microwire arrays were also tested. The assembly process and the structures of the devices are the same as those of NiTPP-C_{60} (Fig. S9a and S10a†). The effective numbers of the microwires between two Au electrodes can be intuitively obtained from SEM images (Fig. S9b and S10b†). As can be seen from the absorption spectrum, C_{60} only shows strong absorption in the ultraviolet region at ~340 nm. Therefore, the photoelectric response characteristics of the C_{60} microwire arrays were measured only at 350 nm UV light on/off (Fig. S9c†). The device showed stable light/dark current during multiple cycle tests, a fast photoresponse of ~0.09 s and a high photocurrent of ~270 nA (Fig. S9d†) at an optical power density of 0.75 mW cm^{-2}. NiTPP has two absorption peaks in the visible light region. Therefore, the photoelectric responses of the NiTPP microwires to blue-violet light at 425 nm and green light at 530 nm were explored. The switching performance of the NiTPP microwire-based photodetector is demonstrated in the *I–T* curve in Fig. S10c–f.† The response is fast, stable and repeatable, showing a response time of ~0.09 s to the pulsed light at 425 nm and ~0.15 s at 530 nm. The photocurrents are ~358 nA at 425 nm under 1.05 mW cm^{-2} optical power density and ~100 nA at 530 nm under 1.14 mW cm^{-2} optical power density. Comparing the results obtained from C_{60}, NiTPP and NiTPP-C_{60}, it was found that molecular engineering by modifying C_{60} with NiTPP not only broadened the light detection range but also enhanced the intensity of photocurrent.

The performances of photodetectors are reflected primarily by the response time and responsivity. Responsivity (*R*) is the photocurrent passing through the effective illumination area of

a detector at unit optical power, which can be expressed by eqn (1):

$$R = \frac{I_l - I_d}{PS} \quad (1)$$

I_l is the photocurrent, I_d is the dark current, P is the optical power density, and S is the effective illumination area of the device. For microwire arrays, the effective illumination area can be calculated using eqn (2):

$$S = L \times W \times n \quad (2)$$

L is the distance between the electrodes, W is the average width of the microwires, and n is the number of effective microwires. The W values of NiTPP-C_{60} microwires can be obtained from Table S1,† and the values of L and n can be obtained from the SEM image of the device in Fig. 4b. The value of S was calculated as 5.84×10^{-5} cm^2, which was then substituted into eqn (1) to plot the responsivity–optical power density curves (R–P) under three light sources (Fig. 6a, c and e). The highest responsivity of the detector under three illuminations is calculated as 8.92 A W^{-1} (350 nm), 11.9 A W^{-1} (425 nm), and 3.11 A W^{-1} (530 nm), respectively. Notably, the responsivity decreases as the optical power density increases (Fig. 6a, c and e) because the responsivity is the ratio of the average output current to the average power of the incident light. The numbers of photoelectrons generated by light excitation will remain unchanged after reaching the maximum, as will the average output current. However, the average power density of the incident light is constantly increasing. Therefore, the R–P curve shows a downward trend, and a similar phenomenon was observed from C_{60} (Fig. S11†) and NiTPP (Fig. S12†) microwire photodetectors. Under the same experimental conditions, the responsivity of the NiTPP-C_{60} microwire photodetector is 2–3 times higher than that of C_{60} and NiTPP photodetectors (Table 1, P_{in}: power density, τ_{on}: rise time, τ_{off}: decay time R: responsivity). This is ascribed to the structural advantage of NiTPP-C_{60}, which provides a transport path for electrons through C_{60} and holes through NiTPP, thereby preventing the recombination of the dissociated electrons and holes. The electrons after being accepted by the fullerene drift rapidly in the microwire under an external electric field. Thus, the D–A heterojunction structure of fullerene and metalloporphyrin can increase the electron mobility and enhance the photoelectric properties.

Response time curves of the NiTPP-C_{60} photodetector under different light sources/power densities are given in Fig. 6b, d and f. A fast photoelectric response was observed during the ascent process (red curve, rise time: 0.08–0.16 s) and the decay process (black curve, decay time: 0.08–0.20 s). The photodetectors based on C_{60} (Fig. S11†) and NiTPP (Fig. S12†) microwire arrays also exhibit fast light response characteristics. The response time mainly relies on the drift velocity of carriers, which is largely affected by the arrangement of molecules within the crystals. Highly ordered molecular arrangement and the fewer defects in the microwires lead to fast movement of the electrons, thereby accelerating the response times. From the analysis and comparison of two crucial performance parameters of the three photodetectors (Table 1), we can draw the following conclusions: (i) the combination of the excellent light absorption characteristics of porphyrin molecules and the good electron transportation properties of fullerene molecules account for the high photocurrent of NiTPP-C_{60}, (ii) the highly

Table 1 The comparison of photoresponse performances of the C_{60}, NiTPP and NiTPP-C_{60} photodetectors

Materials	Light source (nm)	P_{in} [mW cm^{-2}]	τ_{on} (s)	τ_{off} (s)	R [A W^{-1}]
C_{60}	350	0.34	0.09	0.10	4.91
NiTPP	425	0.51	0.20	0.10	4.02
	530	0.41	0.30	0.18	1.34
NiTPP-C_{60}	350	0.34	0.09	0.14	8.92
	425	0.51	0.09	0.10	11.9
	530	0.41	0.11	0.09	3.11

Table 2 Photoelectric performance parameters of fullerene-based broadband photodetectors

Materials	Light source (nm)	P_{in} [mW cm^{-2}]	τ_{on} (s)	τ_{off} (s)	R [A W^{-1}]	Ref.
PDPP$_3$T/PTB$_7$/PC$_{71}$BM	680	—	—	—	0.25	55
	850	—	—	—	0.29	
VTP/PC$_{71}$BM	650	100	0.35	0.4	0.23	56
P$_3$HT/PTB$_7$-Th/PC$_{71}$BM	550	0.016	—	—	0.172	57
PCBM/CsPbBr$_3$	447	3.5	—	—	0.1	58
C_{60}/Cu$_2$O	405	45	0.05	0.01	—	26
	532	45	0.135	0.015	—	
C_{60}/AlClPc	450	—	2.44×10^{-4}	5.48×10^{-4}	94.4	23
	650	—	2.28×10^{-4}	3.79×10^{-4}	3.27	
	808	—	5.02×10^{-4}	6.23×10^{-4}	2.65	
TIPS-PEN/C_{60}	350	1.5	0.78	0.82	165.5	24
	650	1.5	0.91	0.89	149.5	
	720	1.5	0.94	1.21	22.5	
NiTPP-C_{60}	350	0.34	0.09	0.14	8.92	This work
	425	0.51	0.09	0.11	11.6	
	530	0.41	0.11	0.09	3.11	

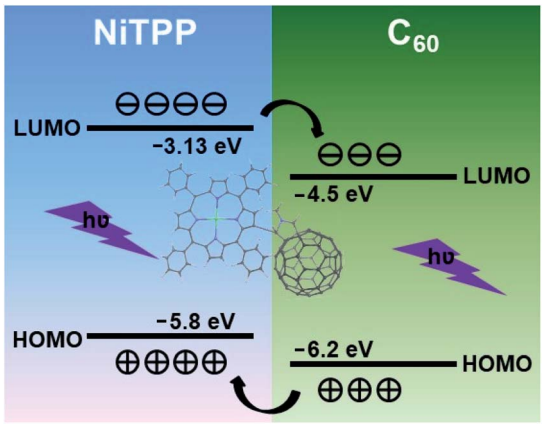

Fig. 7 Energy level diagram and charge transport mechanism of the NiTPP-C_{60} photodetector.

crystalline microwires arrays are responsible for the rapid light response of photodetectors, and (iii) the D–A intramolecular heterojunction facilitates exciton dissociation and charge carrier transportation. The results of fullerene-based broadband photodetectors are compared in Table 2. Our device shows a higher responsivity[55–58] and faster response time[24,56] than most of the fullerene heterojunction devices.

In order to well understand the excellent photodetection performances of the manufactured NiTPP-C_{60} photodetector, a possible mechanism is proposed here. According to the HOMO–LUMO values of C_{60} and NiTPP,[23,59] the energy level diagram of the NiTPP-C_{60} intramolecular heterojunction is shown in Fig. 7. When the NiTPP-C_{60} device was exposed to light, both NiTPP and C_{60} could absorb photons to generate excitons, which quickly dissociated to electrons and holes. The electrons in NiTPP LUMO spontaneously transferred to the LUMO of C_{60}, while the holes remain in the HOMO. The holes generated in C_{60} spontaneously transferred to the HOMO of NiTPP, while the electrons remained in the LUMO. Under an external electric field, electrons generated by light excitation in the D–A molecules can be quickly absorbed by C_{60} and drift rapidly in the highly crystalline microwires to the negative electrode, and holes move along the NiTPP to the positive electrode, thus forming photocurrent, which effectively prevent the recombination of excitons.

3. Conclusion

In summary, a fullerene molecular broadband photodetector was successfully constructed through molecular engineering. The addition of a nickel porphyrin onto the fullerene cage not only broadens the absorption range, but also promotes effective and fast charge carrier transfer. Large-area single-crystal arrays of NiTPP-C_{60} are realized by the liquid bridge induced assembly method, which makes the fabrication of integrated devices possible. The NiTPP-C_{60} broadband photodetector exhibited superior performances, mainly a fast response (350 nm: τ_{on} < 0.09 s; 425 nm: τ_{on} < 0.10 s; 530 nm: τ_{on} < 0.08 s) and high responsivity (350 nm: 8.92 A W^{-1}, 425 nm: 11.6 A W^{-1}, 530 nm: 3.11 A W^{-1}), which are attributed to the high crystallinity, ordered molecular arrangement, efficient exciton dissociation and excellent charge carrier transport properties. This work brings ideas for the design of fullerene-based large-scale broadband photodetectors. By extending the conjugation length of porphyrin, the absorption would be extended from the visible to the NIR region. We believe that molecular engineering represents a general strategy for the preparation of molecules needed for broadband photodetectors.

4. Experimental section

Substrate pre-treatment

The SiO_2 (300 nm)/Si substrate was soaked in a H_2SO_4/H_2O_2 (v/v = 3 : 1) solution for three hours, cleaned with acetone, ethanol, and deionized water, respectively under ultrasonication for ten minutes, and then dried with argon. The treated substrate was immersed in octadecyl trichlorosilane (OTS) solution for half an hour and then dried with a xenon lamp.

Preparation of NiTPP-C_{60}, C_{60} and NiTPP solutions

1 mg, 2 mg and 4 mg NiTPP-C_{60} powder was dissolved in 2 ml of *o*-dichlorobenzene, respectively under ultrasonication for two hours, and then the solution was filtered to obtain clear NiTPP-C_{60} solutions with concentrations of 0.5 mg ml^{-1}, 1 mg ml^{-1} and 2 mg ml^{-1}, respectively. 0.5 mg ml^{-1}, 1 mg ml^{-1} and 2 mg ml^{-1} solutions of C_{60} and NiTPP solutions were prepared by the same procedure.

Preparation of C_{60}, NiTPP and NiTPP-C_{60} microwire arrays

15 μl of each NiTPP-C_{60}, C_{60} and NiTPP solution was gently dropped onto the treated SiO_2/Si substrate. Then, a template was horizontally covered on the substrate to prepare a device, which was placed in an oven at 80 °C for 12 hours.

Photoelectric measurements

A test platform is mainly composed of a probe station, Keithley 2611B source meter, Charge-coupled Device (CCD), display, light source, and TTL signal generator. A combination of the display and the monocular microscope with the CCD can magnify the image of the area between the electrodes of the photodetector, so that the probe can come into contact with the electrodes more accurately. The probe and the photodetector electrodes form a loop which is connected to the Keithley 2611B digital source meter. The source meter provides stable bias voltage and time counting, and collects photocurrent and dark current data of the devices. The TTL signal generator is used to output a square wave signal and connect the light source to control the switch of the light source to obtain data such as photocurrent rise/decay time. Specifically, in this experiment, the gate voltage (VGS) and the bias voltage (VDS) are both set to 10 V. The TTL signal generator was set to provide a square wave signal with a frequency of 0.0005 kHz, which controlled the light source to turn on and off for 1 second, and repeated the cycle.

Conflicts of interest

There are no conflicts to declare.

Acknowledgements

The financial support from the National Natural Science Foundation of China (Grant No. 21672076 and 21971077) and the Graduates' Innovation Fund, Huazhong University of Science and Technology (No. 2020yjsCXCY029) is gratefully acknowledged. The authors acknowledge the facility support of the Analytical and Testing Center in Huazhong University of Science and Technology for all related measurements.

Notes and references

1 J. Clark and G. Lanzani, *Nat. Photonics*, 2010, **4**, 438–446.
2 T. Rauch, M. Böberl, S. F. Tedde, J. Fürst, M. V. Kovalenko, G. Hesser, U. Lemmer, W. Heiss and O. Hayden, *Nat. Photonics*, 2009, **3**, 332–336.
3 K.-J. Baeg, M. Binda, D. Natali, M. Caironi and Y.-Y. Noh, *Adv. Mater.*, 2013, **25**, 4267–4295.
4 M. Kim, H.-J. Ha, H.-J. Yun, I.-K. You, K.-J. Baeg, Y.-H. Kim and B.-K. Ju, *Org. Electron.*, 2014, **15**, 2677–2684.
5 S. Goossens, G. Navickaite, C. Monasterio, S. Gupta, J. J. Piqueras, R. Pérez, G. Burwell, I. Nikitskiy, T. Lasanta, T. Galán, E. Puma, A. Centeno, A. Pesquera, A. Zurutuza, G. Konstantatos and F. Koppens, *Nat. Photonics*, 2017, **11**, 366–371.
6 G. Xiong, T. Minghong, X. Yangjun, C. Wanzhu, M. Ji Sun, C. Yong, Y. Gang, S. Chan-Long, N. Boo and J. H. Alan, *Science*, 2009, **325**, 1665–1667.
7 S. Yang, N. Zhao, L. Zhang, H. Zhong, R. Liu and B. Zou, *Nanotechnology*, 2012, **23**, 255203.
8 J. Qi, L. Ni, D. Yang, X. Zhou, W. Qiao, M. Li, D. Ma and Z. Y. Wang, *J. Mater. Chem. C*, 2014, **2**, 2431–2438.
9 A. Armin, M. Hambsch, I. K. Kim, P. L. Burn, P. Meredith and E. B. Namdas, *Laser Photonics Rev.*, 2014, **8**, 924–932.
10 Z. Chen, Z. Cheng, J. Wang, X. Wan, C. Shu, H. K. Tsang, H. P. Ho and J.-B. Xu, *Adv. Opt. Mater.*, 2015, **3**, 1207–1214.
11 Y. Tao, X. Wu, W. Wang and J. Wang, *J. Mater. Chem. C*, 2015, **3**, 1347–1353.
12 M. Buscema, D. J. Groenendijk, S. I. Blanter, G. A. Steele, H. S. J. van der Zant and A. Castellanos-Gomez, *Nano Lett.*, 2014, **14**, 3347–3352.
13 W. Deng, J. Jie, Q. Shang, J. Wang, X. Zhang, S. Yao, Q. Zhang and X. Zhang, *ACS Appl. Mater. Interfaces*, 2015, **7**, 2039–2045.
14 W. Choi, M. Y. Cho, A. Konar, J. H. Lee, G.-B. Cha, S. C. Hong, S. Kim, J. Kim, D. Jena, J. Joo and S. Kim, *Adv. Mater.*, 2012, **24**, 5902.
15 G. Li, T. Guo, H. Zhang, H. Gao, J. Zhang, B. Liu, S. Yuan, G. Kai and X. Dong, *Appl. Opt.*, 2007, **46**, 283–286.
16 S. D. Stranks and H. J. Snaith, *Nat. Nanotechnol.*, 2015, **10**, 391–402.
17 L. Gao, K. Zeng, J. Guo, C. Ge, J. Du, Y. Zhao, C. Chen, H. Deng, Y. He, H. Song, G. Niu and J. Tang, *Nano Lett.*, 2016, **16**, 7446–7454.
18 X. Zhang, J. Jie, W. Deng, Q. Shang, J. Wang, H. Wang, X. Chen and X. Zhang, *Adv. Mater.*, 2016, **28**, 2475–2503.
19 A. K. Hailey, S.-Y. Wang, Y. Chen, M. M. Payne, J. E. Anthony, V. Podzorov and Y.-L. Loo, *Adv. Funct. Mater.*, 2015, **25**, 5662–5668.
20 W. Deng, X. Zhang, L. Wang, J. Wang, Q. Shang, X. Zhang, L. Huang and J. Jie, *Adv. Mater.*, 2015, **27**, 7305–7312.
21 S. Zheng, X. Xiong, Z. Zheng, T. Xu, L. Zhang, T. Zhai and X. Lu, *Carbon*, 2018, **126**, 299–304.
22 L. Wei, J. Yao and H. Fu, *ACS Nano*, 2013, **7**, 7573–7582.
23 L. Du, X. Luo, F. Zhao, W. Lv, J. Zhang, Y. Peng, Y. Tang and Y. Wang, *Carbon*, 2016, **96**, 685–694.
24 X. Zhao, T. Liu, H. Liu, S. Wang, X. Li, Y. Zhang, X. Hou, Z. Liu, W. Shi and T. J. S. Dennis, *ACS Appl. Mater. Interfaces*, 2018, **10**, 42715–42722.
25 G. Wei, Z. Lu, Y. Cai and C. Sui, *Mater. Lett.*, 2017, **201**, 137–139.
26 B. Cai, Y. Su, J. Hu, C. Zou and Y. Zhang, *J. Mater. Chem. C*, 2018, **6**, 1715–1721.
27 L. Zheng, T. Zhu, W. Xu, L. Liu, J. Zheng, X. Gong and F. Wudl, *J. Mater. Chem. C*, 2018, **6**, 3634–3641.
28 P. Peumans, S. Uchida and S. R. Forrest, *Nature*, 2003, **425**, 158–162.
29 X.-J. Lu, C.-R. Zhang, J.-J. Gong, W. Wang, Z.-J. Liu, Y.-Z. Wu and H.-S. Chen, *Spectrochim. Acta, Part A*, 2020, **242**, 118767.
30 J. Roncali and I. Grosu, *Adv. Sci.*, 2019, **6**, 1801026.
31 S. Hedström, A. J. Matula and V. S. Batista, *J. Phys. Chem. C*, 2017, **121**, 19053–19062.
32 R. S. Kularatne, H. D. Magurudeniya, P. Sista, M. C. Biewer and M. C. Stefan, *J. Polym. Sci., Part A: Polym. Chem.*, 2013, **51**, 743–768.
33 M. Wolf, C. Villegas, O. Trukhina, J. L. Delgado, T. Torres, N. Martín, T. Clark and D. M. Guldi, *J. Am. Chem. Soc.*, 2017, **139**, 17474–17483.
34 S. Vela, S. Bauroth, C. Atienza, A. Molina-Ontoria, D. M. Guldi and N. Martín, *Angew. Chem., Int. Ed.*, 2016, **55**, 15076–15080.
35 M. Rudolf, L. Feng, Z. Slanina, T. Akasaka, S. Nagase and D. M. Guldi, *J. Am. Chem. Soc.*, 2013, **135**, 11165–11174.
36 Y. Shao and Y. Yang, *Adv. Mater.*, 2005, **17**, 2841–2844.
37 R. Charvet, Y. Yamamoto, T. Sasaki, J. Kim, K. Kato, M. Takata, A. Saeki, S. Seki and T. Aida, *J. Am. Chem. Soc.*, 2012, **134**, 2524–2527.
38 Q. Xie, E. Perez-Cordero and L. Echegoyen, *J. Am. Chem. Soc.*, 1992, **114**, 3978–3980.
39 D. M. Guldi, C. Luo, M. Prato, A. Troisi, F. Zerbetto, M. Scheloske, E. Dietel, W. Bauer and A. Hirsch, *J. Am. Chem. Soc.*, 2001, **123**, 9166–9167.
40 S. MacMahon, R. Fong, P. S. Baran, I. Safonov, S. R. Wilson and D. I. Schuster, *J. Org. Chem.*, 2001, **66**, 5449–5455.
41 H. Imahori and Y. Sakata, *Eur. J. Org. Chem.*, 1999, **1999**, 2445–2457.
42 D. M. Guldi, *Chem. Commun.*, 2000, 321–327, DOI: 10.1039/A907807J.

43 C. Larsen, H. R. Barzegar, F. Nitze, T. Wågberg and L. Edman, *Nanotechnology*, 2012, **23**, 344015.
44 X. Zhao, T. Liu, W. Shi, X. Hou, Z. Liu and T. J. S. Dennis, *J. Phys. Chem. C*, 2018, **122**, 8822–8828.
45 X. Zhao, T. Liu, Y. Zhang, S. Wang, X. Li, Y. Xiao, X. Hou, Z. Liu, W. Shi and T. J. S. Dennis, *Adv. Mater. Interfaces*, 2018, **5**, 1800336.
46 K. Liu, S. Gao, Z. Zheng, X. Deng, S. Mukherjee, S. Wang, H. Xu, J. Wang, J. Liu, T. Zhai and Y. Fang, *Adv. Mater.*, 2019, **31**, 1808254.
47 B. Su, S. Wang, J. Ma, Y. Wu, X. Chen, Y. Song and L. Jiang, *Adv. Mater.*, 2012, **24**, 559–564.
48 B. Su, S. Wang, Y. Wu, X. Chen, Y. Song and L. Jiang, *Adv. Mater.*, 2012, **24**, 2780–2785.
49 Y. Wu, X. Chen, B. Su, Y. Song and L. Jiang, *Adv. Funct. Mater.*, 2012, **22**, 4569–4576.
50 D. M. Guldi, I. Zilbermann, G. A. Anderson, K. Kordatos, M. Prato, R. Tafuro and L. Valli, *J. Mater. Chem.*, 2004, **14**, 303–309.
51 Z. Dai, Q. Ou, C. Wang, G. Si, B. Shabbir, C. Zheng, Z. Wang, Y. Zhang, Y. Huang, Y. Dong, J. J. Jasieniak, B. Su and Q. Bao, *J. Mater. Chem. C*, 2019, **7**, 5954–5961.
52 Y. Zhao, X. Fan, J. Feng, X. Wang, Y. Wu, B. Su and L. Jiang, *Adv. Funct. Mater.*, 2018, **28**, 1800470.
53 J. Feng, Q. Song, B. Zhang, Y. Wu, T. Wang and L. Jiang, *Adv. Mater.*, 2017, **29**, 1703143.
54 F. Wang, L. Jia, Y. Ding, H. Cai, W. Zheng and F. Huang, *Small Methods*, 2020, **4**, 2000501.
55 H. Wang, Y. Zheng, R. Qin and J. Yu, *J. Phys. D: Appl. Phys.*, 2018, **51**, 104002.
56 N. A. Roslan, S. M. Abdullah, W. H. A. Majid and A. Supangat, *Sens. Actuators, A*, 2018, **279**, 361–366.
57 J. Miao, F. Zhang, M. Du, W. Wang and Y. Fang, *Adv. Opt. Mater.*, 2018, **6**, 1800001.
58 E.-P. Yao, B. J. Bohn, Y. Tong, H. Huang, L. Polavarapu and J. Feldmann, *Adv. Opt. Mater.*, 2019, **7**, 1801776.
59 C. He, Q. He, C. Deng, L. Shi, D. Zhu, Y. Fu, H. Cao and J. Cheng, *Chem. Commun.*, 2010, **46**, 7536–7538.